Spatiotemporal Monitoring of Melt-Pool Variations in Metal-Based Additive Manufacturing

Hui Yang, Siqi Zhang, Yan Lu, Paul Witherell, and Soundar Kumara

***Abstract*—Additive manufacturing (AM) provides a higher level of flexibility to build customized products with complex geometries, by selectively melting and solidifying metal powders. However, wide applications of AM beyond rapid prototyping are currently limited by its ability to perform quality assurance and control. Advanced melt-pool monitoring provides a unique opportunity to increase information visibility in the AM process. Stochastic melt-pool variations are closely pertinent to the quality of an AM build. There is a pressing need to investigate the variances of melt pools along the temporal scanning path, as well as within a 3D spatial neighborhood of the focal point by the laser beam. This paper presents a stochastic modeling framework to characterize and monitor spatiotemporal variations of melt-pool imaging data, including tensor decomposition of high-dimensional data, additive Gaussian process modeling of low-dimensional profiles as random variables, and hypothesis testing via the construction of confidence boundary for statistical process monitoring. Experimental results show the effectiveness of tensor decomposition for spatiotemporal monitoring of melt-pool variations in the metal-based AM process.**

***Index Terms*—Additive manufacturing, sensor fusion, stochastic modeling, statistical monitoring, spatiotemporal correlation.**

I. Introduction

ADDITIVE manufacturing (AM) provides a higher level of flexibility to produce parts with complex and free-form geometries that are often difficult or even impossible to produce with conventional manufacturing technologies (e.g., subtractive, formative process). To cope with AM complexities, advanced sensing is widely developed and implemented to increase process transparency. As a result, large amounts of time-varying imaging data become readily available. For example, Lane *et al.* designed an integrated monitoring system for the Additive Manufacturing Metrology Testbed (AMMT) at the National Institute of Standards and Technology (NIST) [1]. The AMMT system employs one high-resolution camera and one co-axial high-speed camera to collect melt pool images during the AM process.

Manuscript received 27 February 2022; accepted 22 June 2022. Date of publication 30 June 2022; date of current version 8 July 2022. This paper was recommended for publication by Associate Editor H. Zhang and Editor L. Pallottino upon evaluation of the Reviewers' comments. This work was supported by the National Institute of Standards and Technology under Cooperative Agreement 70NANB19H127. *(Corresponding author: Hui Yang.)*

Hui Yang, Siqi Zhang, and Soundar Kumara are with the Harold and Inge Marcus Department of Industrial and Manufacturing Engineering, The Pennsylvania State University, University Park, PA 16802 USA (e-mail: huy25@psu.edu; suz304@psu.edu; skumara@psu.edu).

Yan Lu and Paul Witherell are with the National Institute of Standards and Technology, Gaithersburg, MD 20899 USA (e-mail: yanlunj@gmail.com; paul.witherell@nist.gov).

Digital Object Identifier 10.1109/LRA.2022.3187540

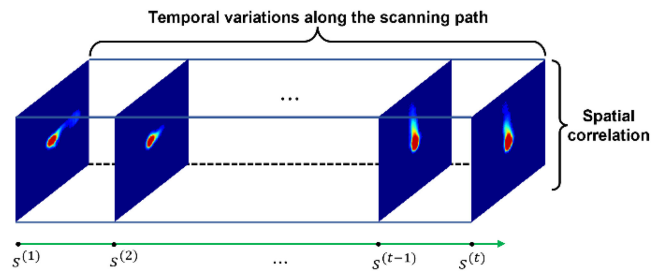

Fig. 1. Spatiotemporal melt-pool imaging data.

As shown in Fig. 1, melt-pool imaging data are both spatially and temporally varying. Each melt pool represents thermal dynamics of laser powder-bed fusion (LPBF) in the underlying AM process at a specific time. In the state of the art, studies tend to focus on monitoring the variations of empirical features (e.g., geometric features) from melt-pool images. Each melt pool is analyzed separately for feature extraction at each time point, which is a conditional method studying the space given time. Little has been done to investigate space-time correlations, e.g., spatial correlation within a melt-pool image, temporal correlation along the scanning path, as well as spatio-temporal interactions.

The evolving dynamics of melt-pool variations are closely pertinent to the quality of a final AM build [2]. However, traditional statistical process control (SPC) methodologies focus primarily on key product metrics or features that represent quality variables, but tend to be limited in the ability to handle complex-structured melt-pool data with spatiotemporal correlations. New analytical tools are needed to handle imaging data and perform the analysis of spatiotemporal variances due to factors (e.g., machine and environment, process parameters, design variables, or materials) in AM. We posit the need for designing stochastic models to overcome these challenges.

This paper presents a stochastic modeling framework to characterize and monitor melt-pool variations through low-dimensional profiles that are extracted via the order-3 tensor transformation of melt-pool imaging data. Specifically, our contributions in this paper are as follows: First, as opposed to traditional black-box approaches, engineering knowledge is integrated with statistical modeling to address assignable factors of melt-pool tail variations (i.e., control and align the melt-pool tails via the available information of laser scanning directions), and then organize time-varying imaging data in an order-3 tensor form. Second, we leverage order-3 tensor decomposition to

extract a sparse set of salient features (i.e., low-dimensional profiles) from high-dimensional melt-pool images, which reduce the computational complexity in the analysis of spatiotemporal variances. Third, a stochastic AGP modeling framework is developed to analyze AM profiles, delineate the variance components, and account for spatiotemporal deviations among different melt pools along the laser scanning path. Finally, both T^2 and generalized likelihood hypothesis testing are designed and formulated for the statistical monitoring of AM processes.

II. Research Background

Advanced imaging has greatly facilitated condition monitoring and quality control of AM processes. The development of various image sensing systems (e.g., infrared camera, high-resolution camera, optical sensors) enables the collection of rich information related to quality characteristics of AM builds. For example, Richter *et al.* [3] leveraged a high-speed X-ray imaging system to investigate melt dynamics during continuous-wave laser remelting of Co-Cr alloy. Furumoto *et al.* [4] used a high-speed digital imaging apparatus to investigate melt pool behavior and the characteristics of surrounding metal powder during the laser powder bed fusion (LPBF) process. See a detailed review on AM sensing systems and quality management in [5].

The increasing availability of imaging data has fueled growing interests in the development of image-guided SPC methods. For example, Kan *et al.* [6] designed a dynamic network framework for statistical monitoring of time-varying imaging data from ultra-precision machining and bio-manufacturing processes. Zhang *et al.* [7] presented a nonparametric AGP model to quantify variations in surface profiles of silicon wafers and monitor the quality of final products. Further, in the domain of metal AM, Caggiano *et al.* [8] investigated machine learning algorithms for image processing and defect detection in Selective Laser Melting (SLM) of metal powders. Yao *et al.* [9] proposed a multifractal methodology to characterize and identify layerwise defects from AM imaging data. Lindenmeyer *et al.* [10] presented a template-based and Bayesian reasoning approach to characterize geometric shape and size of the melt pool. Scime *et al.* [11] combined machine learning techniques with empirical gradient features to classify melt-pools and predict flaws. Deep neural networks were also utilized to characterize melt-pool sizes and identify melt pools with spatter and plume [12]. Deep learning treats an AM process as a black-box, and thus cannot adequately model the image as random variables with standard profile and random deviations. In contrast, statistical modeling relies on engineering knowledge and sensing data to provide a mathematical representation of variance components in AM.

Because a single melt-pool image is in the 2-dimensional space, temporal information is embedded when a sequence of melt-pool images is collected. Thus, most of existing methods handle the spatiotemporal information to some extent with a variety of approaches. Nonetheless, in the state of the art, most of previous studies tend to focus on monitoring the variations of empirical features (e.g., geometric features) from melt-pool images. Each melt pool is analyzed separately for feature extraction at each time point. Then, the temporal variation of features is modeled with different approaches. For example, Moges *et al.* [13] proposed a hybrid modeling approach to combine physics-based, simulation data, and imaging data for the prediction of melt-pool width (i.e., a feature descriptor extracted from melt-pool images). Zhuo *et al.* [14] developed a neighboring-effect modeling method to characterize spatiotemporal melt-pool images for the prediction of melt-pool size (i.e., another feature descriptor).

Despite recent advances, little has been done to handle order-3 tensor form of melt-pool imaging data and perform the stochastic modeling and analysis of spatiotemporal variances. Opportunities exist to leverage low-dimensional profiles and the AGP to model variance components in the AM process. AGP modeling helps delineate standard patterns, spatiotemporal variation components from random noises, and further facilities the formulation of hypothesis tests for anomaly detection in AM.

III. Research Methodology

A. Image Alignment to Address Assignable Factors

Engineering knowledge (e.g., laser scanning path) is critical to pre-process and align melt-pool imaging data, which can help address the assignable factors of melt-pool tail variations. Note that a melt pool often has a tail along the laser scanning direction during the AM process. When the laser is scanning along different paths, tail directions of melt pools also vary accordingly. Such misalignment of tail directions can pose great challenges to the characterization and monitoring of melt-pool variations. It is just not wise to feed unaligned melt-pools into Artificial Intelligence (AI) tools, and then let AI take care of all the work (e.g., alignment, decomposition, modeling, monitoring). Hence, we leverage linear affine transformation to find a mapping between a melt-pool image and its aligned counterpart at a rotated angle, which can be described as follows,

$$\begin{bmatrix} \tilde{x} \\ \tilde{y} \end{bmatrix} = \begin{bmatrix} \cos(\theta) & -\sin(\theta) \\ \sin(\theta) & \cos(\theta) \end{bmatrix} \begin{bmatrix} x \\ y \end{bmatrix} \tag{1}$$

where (x, y) represents a 2-D vector and θ is the rotation angle. The melt-pool tail direction is related to the laser scanning direction. Then, the rotation angle is estimated by transforming the laser scanning direction into the target direction $(\tilde{x}, \tilde{y})$. For a given laser focal point $(x^{(t)}, y^{(t)})$ at time t, each melt-pool image can be aligned into a consistent direction based on the gradient vector of the laser scanning path. After alignment, the stream of melt-pool imaging data is organized as an order-3 tensor $\mathcal{M} \in \mathbb{R}^{I_1 \times I_2 \times T}$, where I_1 and I_2 are the x- and y- dimensionality of a melt-pool image, T is the total number of melt-pool images over time.

B. Tensor Decomposition of Melt-Pool Imaging Data

Tensor decomposition helps preserve the underlying structure in original data and transforms high-dimensional data into a low-dimensional space. Principal component analysis (PCA) is commonly used for order-2 data, but cannot handle order-3

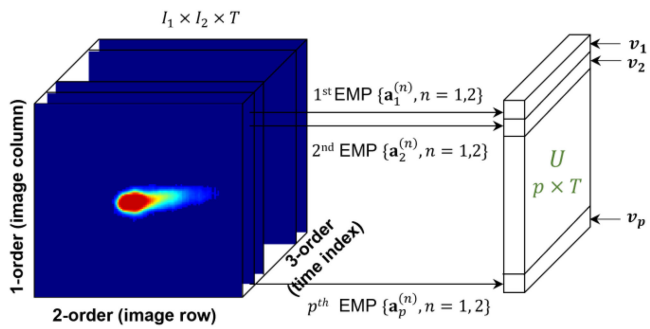

Fig. 2. Tensor decomposition of melt-pool imaging data.

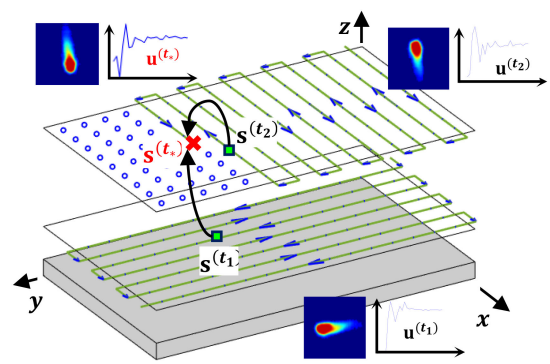

Fig. 3. Spatiotemporal correlations in AM.

tensor data. Traditional PCA is applied on vectorized imaging data, which tend to lose inherent structures and correlations in the order-3 tensor data. Therefore, we propose tensor decomposition, also called tensor-to-vector projection (TVP), to derive uncorrelated features from melt-pool images. These low-dimensional feature vectors are not only orthogonal to each other but also maximize projection variances. The TVP consists of multiple elementary multilinear projections (EMPs), which project a tensor $\mathcal{M} \in \mathbb{R}^{I_1 \times I_2 \times \ldots \times I_N}$ to a scalar u through N projection vectors as

$$u = \mathcal{M} \times_1 \mathbf{a}^{(1)'} \times_2 \mathbf{a}^{(2)'} \ldots \times_N \mathbf{a}^{(N)'} \tag{2}$$

where $\mathbf{a}^{(n)}$ is the n-th projection vector, $\mathbf{a}^{(1)'}$ is the transpose of $\mathbf{a}^{(1)}$, and $\times_n$ is the n-th mode product. Note that the n-mode product of tensor $\mathcal{M}$ and a matrix A is equivalent to $A\mathcal{M}_{(n)}$, where $\mathcal{M}_{(n)}$ is the unfolding matrix of tensor data along the n-th dimension. Fig. 2 illustrates tensor decomposition of melt-pool imaging data $\mathcal{M}$ into a two-dimensional matrix U as

$$U = \mathcal{M} \times_1 \mathbf{a}_p^{(1)'} \times_2 \mathbf{a}_p^{(2)'} \tag{3}$$

where p is the index of EMP, $U = [\mathbf{u}^{(1)}, \ldots, \mathbf{u}^{(T)}]$ and $\mathbf{u}^{(t)} = [u_1, \ldots, u_p|t]'$. The $u_p^{(t)}$ is the projection of t-th melt-pool image from the p-th EMP, and $v_t^{(p)}$ represents the p-th coordinate and $u_p^{(t)} = v_t^{(p)}$. The objective of tensor decomposition is to maximize the variance of projections under constraints imposed on the EMPs, see algorithmic details in our previous work [15].

C. Stochastic Modeling of Tensor Profiles With AGP

Tensor decomposition transforms each melt-pool image (i.e., in the dimensionality of $I_1 \times I_2$) into a low-dimensional profile (i.e., $\mathbf{u}^{(t)} = [u_1, \ldots, u_p|t]'$). For an order-3 tensor $\mathcal{M} \in \mathbb{R}^{I_1 \times I_2 \times T}$ with T melt-pool images, we have

Time	Melt-pool	Low-dimensional tensor profile
t=1	Image ($I_1 \times I_2$)	$\mathbf{u}^{(1)} = [u_1, \ldots, u_p\|t = 1]'$, a p×1 vector
t=2	Image ($I_1 \times I_2$)	$\mathbf{u}^{(2)} = [u_1, \ldots, u_p\|t = 2]'$, a p×1 vector
⋮	⋮	⋮
t=T	Image ($I_1 \times I_2$)	$\mathbf{u}^{(T)} = [u_1, \ldots, u_p\|t = T]'$, a p×1 vector

Due to process and measurement uncertainty, these low-dimensional profiles show standard patterns but with variations due to assignable and/or unassignable causes. These variations can occur over time $\mathbf{u}^{(t)}$, $t = 12, \ldots, T$ or along the feature index p $[u_1, \ldots, u_p|t]$ at a given time t. There is an urgent need to delineate variation components in tensor profiles $\mathbf{u}^{(1)}, \ldots, \mathbf{u}^{(t)}$. With LPBF, as shown in Fig. 3, metal powders are spread and melted in the layer-by-layer fashion, creating complex spatial and temporal correlations. For example, melt-pool formation at a given location $s^{(t_*)}$ is influenced by adjacent regions either within the same layer (i.e., $s^{(t_2)}$) or across the layer (i.e., $s^{(t_1)}$).

Therefore, we propose an additive Gaussian process modeling framework to analyze AM profiles, delineate the variance components, and account for spatiotemporal deviations among different melt pools along the laser scanning path. The proposed AGP modeling entails the addition of two GPs with different covariance structures, which facilitates the design of hypothesis tests for statistical monitoring of AM processes. As shown in Eq. (4). The first GP estimates the standard profile, while the second GP aims to capture spatiotemporal correlations in adjacent regions (i.e., either within the same layer or across the layer as shown in Fig. 3) in the AM process.

$$u_p^{(t)} = f(p) + g\left(p, \mathbf{s}^{(t)}\right) + \varepsilon \tag{4}$$

where t is the time index of image data, $u_p^{(t)}$ is the p-th feature of the tensor profile $\mathbf{u}^{(t)}$ at time t, ε is the random noise, and $\mathbf{s}^{(t)} = [x^{(t)}, y^{(t)}, z^{(t)}]$ denotes spatial coordinates (in units: mm) of the t-th melt-pool image.

The standard profile $f(p)$ is modeled as a Gaussian process with mean μ and covariance function $K_f(p, \tilde{p})$. The deviation term $g(p, \mathbf{s}^{(t)})$ is modeled as the second Gaussian process with mean 0 and covariance function $K_g(\Phi, \tilde{\Phi})$, where $\Phi = [p, \mathbf{s}^{(t)}]$, accounting for both feature covariances and spatiotemporal covariances in adjacent regions. As such, tensor profile $\mathbf{u}^{(t)}$ from t-th melt-pool image is modeled as the addition of two GPs with covariance structures as follows:

$$K_f\left(p, \tilde{p}|\sigma_f, l_f\right) = \sigma_f^2 \exp\left[-\frac{(p - \tilde{p})^2}{2l_f^2}\right] \tag{5}$$

$$K_g\left(\Phi, \tilde{\Phi}|\sigma_g, l_g\right) = \sigma_g^2 \exp\left[-\frac{\left(\Phi - \tilde{\Phi}\right)^2}{2l_g^2}\right] \tag{6}$$

where l_f and $l_g$are the correlation parameter, σ_f^2 and σ_g^2 are the signal variance. The additive covariance function becomes $K\left(\Phi, \tilde{\Phi}\right) = K_f\left(p, \tilde{p}\right) + K_g(\Phi, \tilde{\Phi})$. It may be understood in the way that AGP is a GP with two distinct covariance structures so as to delineate variation components.

The collection of $\mathbf{U} = [\mathbf{u}^{(1)}; \mathbf{u}^{(2)}; \cdots; \mathbf{u}^{(T)}]$ contains the set of tensor profiles for melt-pool images collected at different time indices. Let $\Omega = [\mu, \sigma_f, \sigma_g, l_f, l_g]$ be the parameter set of the AGP model. Then, the parameter set $\hat{\Omega}$ can be estimated by maximizing the log-likelihood function of in-control data,

$$\hat{\Omega} = \arg\max_{\Omega} \left\{ \begin{array}{c} -\frac{1}{2} log\left(\left|K\left(\Phi, \Phi\right) + \sigma^2 I\right|\right) - \frac{1}{2}\left(\mathbf{U} - \mu \mathbf{1}_{PT}\right)' \\ \left(K\left(\Phi, \Phi\right) + \sigma^2 I\right)^{-1}\left(\mathbf{U} - \mu \mathbf{1}_{PT}\right) \end{array} \right\} \tag{7}$$

The AGP model is trained to approximate the standard profile and quantify correlated deviations in the in-control data set $\mathbf{U}$. If the process is in control (i.e., the null hypothesis is true), then the tensor profile of a new melt pool $\mathbf{u}*$ will follow a joint Gaussian distribution with the in-control data set $\mathbf{U}$ as:

$$\begin{bmatrix} \mathbf{U} \\ \mathbf{u}^* \end{bmatrix} \sim N\left(\begin{bmatrix} \mu \mathbf{1}_{PT} \\ \mu \mathbf{1}_P \end{bmatrix}, \begin{bmatrix} K\left(\Phi, \Phi\right) + \sigma^2 I & K\left(\Phi, \phi^*\right) \\ K\left(\phi^*, \Phi\right) & K\left(\phi^*, \phi^*\right) + \sigma^2 I \end{bmatrix}\right) \tag{8}$$

The posterior distribution of $\mathbf{u}^*$is given by

$$\mathbf{u}^* | \mathbf{U}, \Phi, \phi^* \sim N\left(\hat{\mu}_{\mathbf{u}^*}, \hat{\Sigma}_{\mathbf{u}^*}\right) \tag{9}$$

where

$$\hat{\mu}_{\mathbf{u}^*} = \mu \mathbf{1}_P + K\left(\phi^*, \Phi\right)\left(K\left(\Phi, \Phi\right) + \sigma^2 I\right)^{-1}\left(\mathbf{U} - \mu \mathbf{1}_{PT}\right) \tag{10}$$

$$\begin{aligned} \hat{\Sigma}_{\mathbf{u}^*} = & K\left(\phi^*, \phi^*\right) + \sigma^2 I - K\left(\phi^*, \Phi\right) \\ & \times \left(K\left(\Phi, \Phi\right) + \sigma^2 I\right)^{-1} K\left(\Phi, \phi^*\right) \end{aligned} \tag{11}$$

Hence, AGP provides uncertainty quantification of a new melt pool, which facilitates the design and formulation of hypothesis tests for anomaly detection in the AM process.

D. Statistical Monitoring

Further, we design Hotelling T^2 and generalized likelihood ratio (GLR) hypothesis testing for statistical monitoring of AM processes. When a melt-pool image is normal, the profile $\mathbf{u}^*$ from a melt-pool image is expected to fall into an uncertainty band that is quantified from the AGP model. Therefore, null and alternative hypotheses are formulated as follows,

$$H_0: \mathbf{u}^* \sim N\left(\hat{\mu}_{\mathbf{u}^*}, \hat{\Sigma}_{\mathbf{u}^*}\right) \quad H_1: \mathbf{u}^* \not\sim N\left(\hat{\mu}_{\mathbf{u}^*}, \hat{\Sigma}_{\mathbf{u}^*}\right)$$

The Hotelling T^2 statistic is $\lambda_{T^2} = \left(\mathbf{u}^* - \hat{\mu}_{\mathbf{u}^*}\right)' \left(\hat{\Sigma}_{\mathbf{u}^*}\right)^{-1} \left(\mathbf{u}^* - \hat{\mu}_{\mathbf{u}^*}\right)$. The upper control limit of the T^2 statistic is χ_p^2, where χ_p^2 is the upper 100 $\alpha\%$ of a Chi-distribution with a degree of freedom of p. When λ_{T^2} is larger than the UCL, we reject H_0 , indicating that the melt-pool image is abnormal. Otherwise, we fail to reject the null hypothesis and no significant variations exist in the melt pool.

Further, we formulate a GLR test to determine whether stochastic deviations exist from the out-of-control. Common variations include melt-pool sizes, irregular shapes, and spatters. These shifts can result in mean and variance shifts in the tensor profiles. Hence, we assume that an assignable cause adds the third deviation term $h(p, \mathbf{s}^{(t)})$ to the AGP model, leading to

$$u_p^{(t)} = f\left(p\right) + g\left(p, \mathbf{s}^{(t)}\right) + h\left(p, \mathbf{s}^{(t)}\right) \tag{12}$$

For consistency, this term is modeled as a GP with a mean of μ_h and covariance function Σ_h in the form of squared exponential covariance function $\left(\text{i.e., } \sigma_h^2 \exp\left[-\frac{\left(\Phi - \tilde{\Phi}\right)^2}{2 l_h^2}\right]\right)$. As a result, the hypothesis for the GLR test becomes,

$$H_0: \mathbf{u}^* \sim N\left(\hat{\mu}_{\mathbf{u}^*}, \hat{\Sigma}_{\mathbf{u}^*}\right)$$

$$H_1: \mathbf{u}^* \not\sim N\left(\hat{\mu}_{\mathbf{u}^*} + \mu_h \mathbf{1}_P, \hat{\Sigma}_{\mathbf{u}^*} + \Sigma_h\right)$$

This hypothesis is equivalent to testing whether a specific type of shift exists, and therefore we can also get pertinent information about the root cause. The GLR statistic can be described by

$$\lambda_{GLR} = 2 \ln \frac{\sup_{\vartheta} \mathcal{L}\left(H_1\right)}{\mathcal{L}\left(H_0\right)} \tag{13}$$

where $\vartheta = [\mu_h, \sigma_h, l_h]$ is the set of parameters for the third GP and $\mathcal{L}$ is the likelihood ratio function. When λ_{GLR} exceeds the limit, null hypothesis H_0 is rejected and there are significant variations in the melt pool.

IV. Experimental Design and Results

A. Simulation Study

We first evaluate and validate the performance of AGP model with simulation experiments on the use of complex functions as thermal profiles. Based on the assumption of AGP model, each thermal profile consists of two components, i.e., the standard profile and the spatiotemporal deviation term. Hence, we simulate the standard profile with a mathematical function as follows,

$$\eta\ (p) = \sin\left(4p\right) + \cos\left(10p\right) + e^p + 2 \tag{14}$$

where p is the normalized index ranging from 0 to 1. The spatiotemporal deviation term is simulated with a Gaussian process with parameters of $\sigma_g^2 = 0.05^2$ and $l_g = 0.2$ in Equation (6). The spatial locations $\mathbf{s}^{(t)}$ of 50 melt pools come from a 5×10 mesh grid, and the grid size is 0.1. Then, 50 thermal profiles are generated and then utilized to estimate the AGP model and construct the confidence boundary for new thermal profiles. We assume that the function form of thermal profiles is not available. Instead, only samples are drawn from each profile based on the Latin hypercube sampling strategy.

AGP offers an attractive feature to delineate variation components using the addition of GPs with different covariance structures. This is similar to Analysis of Variance (ANOVA) in traditional statistics but is instead realized with GPs for melt-pool images. Specifically, the stream of low-dimensional AM tensor profiles is modeled as the addition of two GPs. The

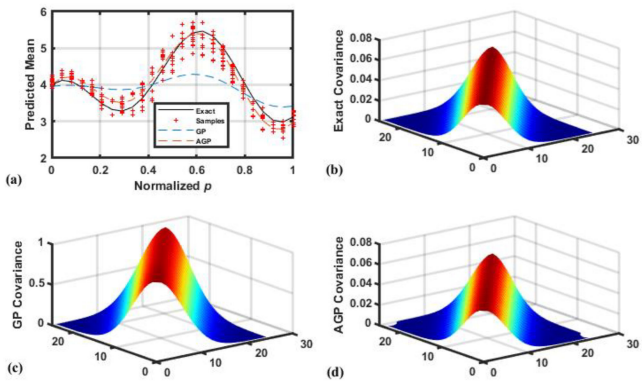

Fig. 4. Predicted mean and covariance functions from GP and AGP models: (a) Samples, exact and predicted mean functions, (b) ground truth covariance, (c) GP predicted covariance, and (d) AGP predicted covariance.

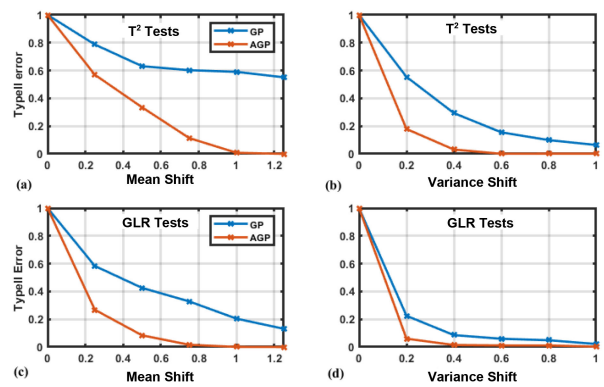

Fig. 5. Performance comparison of type II errors for T^2 tests under different magnitudes of (a) mean and (b) variance shifts, as well as for GLR tests under different magnitudes of (c) mean and (d) variance shifts.

first GP estimates the standard profile while the second GP aims to capture spatiotemporal variations, thereby delineating variation components in the data. As a benchmark to the AGP model, we also evaluated a traditional GP model that does not design the addition of GPs to delineate variation components, which is formulated as a noisy GP model, $u_p^{(t)} = \zeta(p,\ \mathbf{s}^{(t)}) + \varepsilon$. Note that this GP model employs a single Gaussian process to approximate the tensor profile and assumes random noises for modeling the deviations.

Fig. 4(a) shows the exact mean, samples, as well as predicted mean functions from both the noisy GP and AGP models. Notably, the GP model reports a larger deviation from the ground truth than AGP model. Fig. 4(b)–(d) shows the ground truth of covariance, as well as predicted covariance functions from GP, and AGP models. Although the shape of GP-predicted covariance is similar to that of exact covariance, its values are significantly larger than that from the exact function. This is due to the fact that the GP model only considers interrelations between spatial coordinates and indices of the curve but not the standard shape described by the index p. Instead, the AGP-predicted covariance is close to the ground truth of covariance in terms of both the shape and values. Hence, the proposed AGP framework yields better performance than the GP for approximating complex curves with both the standard pattern and spatiotemporal deviation term.

Next, we evaluate the performance of proposed statistical monitoring approaches for these simulated profiles. Note that each experiment is randomly replicated 100 times. First, 50 thermal profiles are generated as in-control data to estimate the AGP model. Then, a total of 25 new profiles from an out-of-control process are generated based on the formulation of $h(p,\ \mathbf{s}^{(t)})$, i.e., Equation (12) in Section III.D. Lastly, both T^2 and GLR tests are performed to determine whether a new profile is in conformance with the established confidence boundary. Type II error is used as the operational characteristic to compare the performance of different hypothesis testing approaches. The control limits for both tests are based on the significance level of 0.05.

Fig. 5 shows the variations of operational characteristic curves to compare the performance for both noisy GP and AGP models in terms of type II errors under different magnitudes of mean and variance shifts. Note that both models are capable of detecting the mean and variance shifts. However, the AGP model outperforms the GP model in terms of type II error at any given magnitude of mean and/or variance shifts. When comparing the T^2 test with the GLR test, the latter performs better in detecting the mean and variance shift. Overall, the GLR test with the stochastic AGP framework shows superior performance to identify anomaly conditions in different scenarios of mean and variance shifts.

B. *Real-World Case Study*

The proposed AGP methodology is further applied and evaluated for monitoring stochastic variations of melt-pool images from a laser-powder-bed-fusion build, which are open-access data from the National Institute of Standards and Technology (NIST) [16]. Each melt-pool image has 120×120 pixels with the pixel value ranging from 0 to 255. A serpentine scan strategy is used for this build, which results in different laser moving directions.

The ground truth is established on the basis of changes (or anomalies) in process conditions such as changes in laser powers, scanning directions, spatters, and melt-pool shapes. These changes are either encoded in the machine commands or visually identified by AM experts (e.g., spatters). Fig. 6(a)-(b) shows melt-pool images when the laser power is reduced from 195W to 100W and the direction of laser moving path is $-90\,^{\circ}$. As the laser power decreases, the size of melt pools becomes smaller. Fig. 6(c)-(d) shows melt-pool images when the direction of laser scanning path is changed from top-down (-90°) to bottom-up ($+90^{\circ}$). Note that melt-pool tails are influenced by the laser moving direction, calling upon image alignment (i.e., Section III.A) to address this assignable factor instead of leaving the work as a black-box to AI. Further, we show the normal patterns (i.e., Fig. 6(i)-(ii)) and abnormal variations (i.e., Fig. 6(iii)-(iv)) of melt-pool images when the laser power is 195W and the directional angle is -90°.

Fig. 7(a) shows the patterns of tensor-decomposed profiles and stochastic variations under different process conditions. Tensor profiles $\mathbf{u}^{(t)}$ from normal melt-pool images

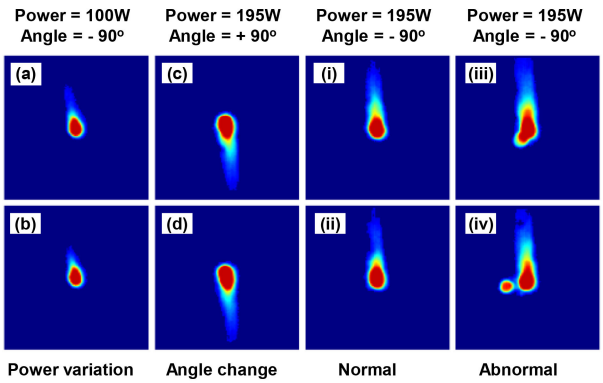

Fig. 6. Sample melt-pool images under different process conditions and variations: (a-b) power = 100 W, directional angle = - 90° , (c-d) power = 195 W, directional angle = + 90 ° , (i-ii) power = 195W, directional angle = - 90 ° , normal conditions, (iii-iv) power = 195 W, directional angle = - 90 ° , abnormal conditions (also see Figs. 7(a) and 8).

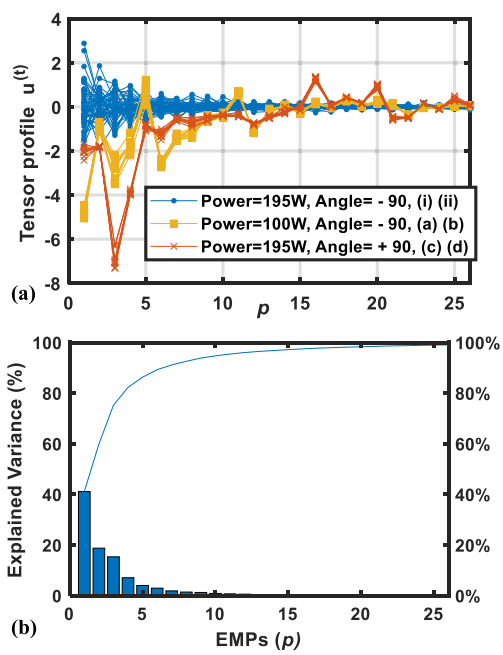

Fig. 7. (a) The variations of tensor-decomposed profiles w.r.t. process conditions; (b) Pareto chart of the percentage of explained variations w.r.t. the dimensionality of p in the tensor profile.

(see Fig. 6(i)-(ii)) tend to fluctuate between -3 to 3 and $u_p^{(t)}$ goes to 0 when the feature index p becomes large. However, tensor profiles show different behaviors when process conditions change. The change in laser power leads to higher levels of oscillations (1<p<12) in tensor profiles. The change in direction angles gives even larger variances in tensor profiles. These results show that low-dimensional profiles ($\mathbf{u}^{(t)} = [u_1, \ldots, u_p|t]'$ ', a p×1 vector, t = 1,…,T) extracted from the order-3 tensor $\mathcal{M} \in \mathbb{R}^{I_1 \times I_2 \times T}$ of melt-pool images are salient features sensitive to process variations.

The tensor projection index p is a critical parameter that is used as inputs for Gaussian process modeling. The selection criterion is to identify an optimal number of EMPs p that can

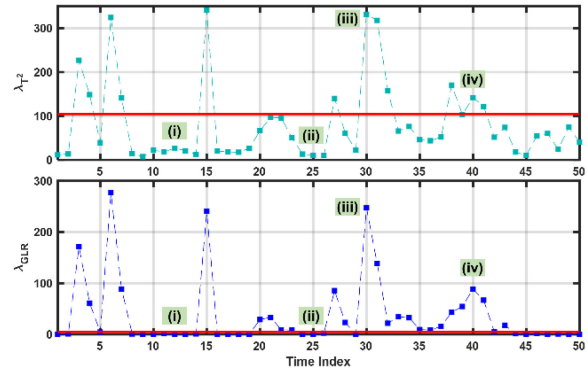

Fig. 8. Hotelling T^2 and GLR test statistics for AM tensor profile monitoring.

explain the majority of variations (e.g., $\geq 99\%$) in the melt-pool images. Therefore, we performed the experiments to evaluate how the number of EMPs (i.e., the dimensionality p of a tensor profile $\mathbf{u}^{(t)}, t = 1, \ldots, T$) impacts the percentage of explained variations in melt-pool images. As shown in Fig. 7(b), the first feature (i.e., $p = 1$) explains around 40% of total variance, and the first 26 features can account for 99% of total variance. Further decomposition tends to only capture extraneous noises in 1% of data variances. Hence, we choose p = 26 as the total number of features in the tensor decomposition. As a result, each melt-pool image of size $I_1 \times I_2$ is transformed into a 26-variate vector $\mathbf{u}^{(t)}$.

Next, we evaluate the proposed AGP framework for statistical monitoring of melt-pool variations through low-dimensional tensor profiles. The AGP models tensor profiles as a stochastic function and then formulates both T^2 and GLR tests to determine whether a new profile is beyond the confidence interval. As shown in Fig. 8, both T^2 and GLR tests effectively capture abnormal variations in melt-pool images. T^2 test reports 12 abnormal profiles with larger statistics than UCL, while the GLR test is more sensitive with a lower UCL to report 13 anomalies. Abnormal images that fail the hypothesis test are shown in Fig. 6(iii)-(iv). Note that these melt pools display significant variations (i.e., geometric shape, size, spatter) from normal melt pools in Fig. 6(i)-(ii). Experimental results show that the proposed AGP framework shows great potentials for statistical monitoring of stochastic variations in the melt-pool imaging data.

V. Discussion

The characteristics of melt pools are highly correlated to the final quality of AM builds. In-situ monitoring of melt pools is critical to achieving quality assurance and process repeatability of AM process. However, there are practical issues pertinent to the monitoring of melt-pool characteristics during the process, e.g., high-dimensional melt-pool imaging data, how different process parameters (i.e., laser power) influence melt-pool characteristics, and how the formation of melt-pool is influenced by the spatiotemporal neighborhood.

This paper proposed a stochastic modeling framework for statistical modeling and monitoring of melt-pool imaging data,

including tensor decomposition of high-dimensional data, additive Gaussian process modeling of low-dimensional profiles as stochastic functions, and hypothesis testing via the construction of confidence boundary. Note that traditional feature-based approaches are more concerned about the extraction of characteristic features and then formulate classification and clustering problems for the identification and detection of AM defects. Instead, this paper focuses on modeling image profiles as stochastic functions and then formulating the hypothesis testing problem for statistical monitoring of AM processes. The proposed framework shows great potentials to represent and analyze melt-pool imaging data for process monitoring in AM machines.

The proposed framework provides attractive features as follows: 1) Dimensional reduction: The tensor decomposition algorithm not only transforms time-varying imaging data from a high-dimensional space into low-dimensional profiles, but also preserves interrelationships among such low-dimensional profiles representing different melting locations along the scanning path. 2) Confidence boundary: Because the AGP model estimates both mean and covariance matrix for new profiles, a confidence boundary can be constructed for the hypothesis testing.

However, a purely statistical method tends to encounter several limitations, e.g., the consideration of variations in the actual part geometry under various scanning patterns and process settings. Under those scenarios, physics-informed statistical methods may be more suitable and practical. In the literature, physics-based models have also been explored to study melt-pool characteristics. Olleak *et al.* [17] proposed an integrated framework of finite element and data-driven modeling for predictions of melt pools of the selective laser melting process. Traditional data-driven methods are more concerned about data assimilation, information extraction, and statistical modeling [18]. Instead, physics-informed methods account for physics or kinetic simulation models which may only require a small dataset for model calibration and validation [19]. In our future work, we will further investigate the integration of physical related parameters with the AGP model to leverage low-dimensional profiles for AM process monitoring and control.

Furthermore, the proposed framework is embodied by two phases, as shown in Fig. 9.

1) *In-control learning:* This phase leverages in-control data to learn the AGP model and estimate both mean and covariance matrix for the construction of confidence boundary to test a new melt-pool image.

2) *Anomaly detection:* The learned AGP model is used to perform hypothesis testing for statistical monitoring of AM processes. Please see below for benchmark experiments to compare the running times of each phase.

In-control learning: First, we evaluated the running time of tensor decomposition on a random sample of 100 melt-pool images and replicated this experiment for 100 times on different samples. As shown in Fig. 10(a), it takes approximately16 to 24 seconds to perform tensor decomposition with an average of 19.92 seconds and a standard deviation of 1.22 seconds. The tensor decomposition transforms time-varying imaging data

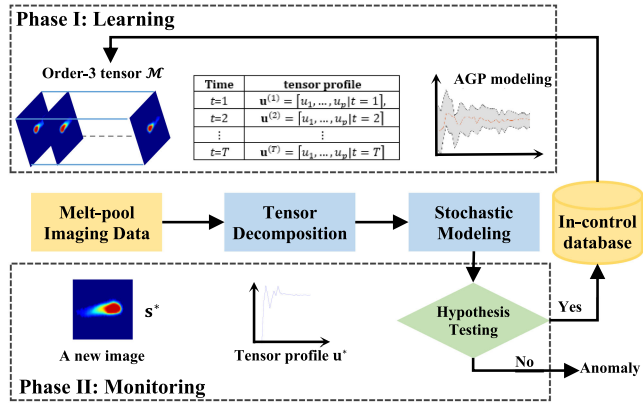

Fig. 9. Flowchart of the proposed modeling framework.

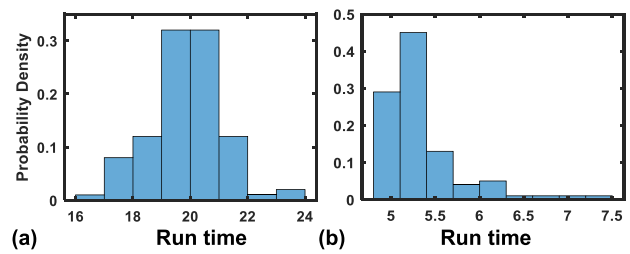

Fig. 10. The distribution of running time for (a) tensor decomposition and (b) AGP modeling of an in-control sample of 100 melt-pool images.

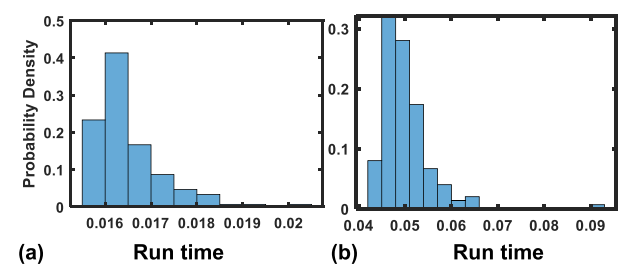

Fig. 11. The distribution of running time for online (a) tensor decomposition and (b) hypothesis testing for a sequence of 150 new melt-pool images.

from a high-dimensional space into low-dimensional profiles, which addresses the "curse of dimensionality" issue in melt-pool images. In other words, the computational complexity in stochastic AGP modeling of low-dimensional profiles is much lower than direct modeling of melt-pool images. Second, we also performed experiments for running time comparisons in AGP modeling and learning of tensor profiles. The average is approximately 5.33 seconds and the standard deviation is about 0.45 seconds, also see Fig. 10(b). Overall, it takes an average of ∼25.25 seconds for tensor decomposition and AGP learning with an in-control sample of 100 melt-pool images.

Anomaly detection: When a new melt-pool image comes, the learned AGP model will be used to perform the hypothesis testing via the construction of confidence boundary. Also, we perform benchmark experiments to evaluate run times on tensor decomposition and hypothesis tests in a sequence of 150 new melt-pool images. Experimental results show that it takes an average of 0.0165 seconds to transform one image into a low-dimensional tensor profile, also see Fig. 11(a). This processing

time is much faster than that of in-control learning due to projection vectors that are already learned in the first phase. Then, it takes an average of 0.05 seconds to perform hypothesis testing and check the conformance of a new tensor profile, also see Fig. 11(b). The computation time is estimated with the use of a desktop computer with Intel Xeon 3.50GHz, 32GB RAM, and can be further improved with parallel-computing workstations [20]. In our case study, the run time shows promise to be implemented for the purpose of real-time monitoring. It may also be noted that there are different ways to further increase the computational efficiency of proposed modeling framework. For example, when a new melt-pool image passes the hypothesis testing and is then added into in-control database, a block-wise matrix inversion and fully independent training conditional (FITC) approximation [21], [22] can be used for faster update of AGP models based on sequential sampling of data.

VI. Conclusion

Statistical monitoring of melt pools is critical to achieving quality assurance and process repeatability for AM. However, there are practical issues pertinent to the monitoring of melt-pool characteristics during the process, e.g., the curse of dimensionality in melt-pool images, open-box vs. black-box approaches, empirical features vs. statistical modeling, as well as spatially and temporally dependent correlations. This paper presents a stochastic modeling framework to characterize and monitor melt-pool variations through low-dimensional representations of melt-pool imaging data. First, we align melt-pool imaging data based on the engineering knowledge of a laser scanning path, then model time-varying imaging data as an order-3 tensor to preserve spatiotemporal correlations among imaging data collected at different spatial locations. Second, we utilize the tensor decomposition algorithm to extract a sparse set of salient features from high-dimensional tensor data. Third, an AGP framework is proposed to capture the standard pattern of AM tensor profiles and the spatial-temporal dependence. Finally, T^2 and GLR tests are designed to test the hypothesis that a new melt pool conforms to its predictive distribution from the AGP model. Experimental results show that the proposed methodology has strong potentials for statistical monitoring and control of melt-pool variations. Our future research will focus on studying low-dimensional profiles under different part geometries and how these variations can be modeled for AM process monitoring and control.

References

[1] B. Lane *et al.*, "Design, developments, and results from the NIST additive manufacturing metrology testbed (AMMT)," in *Proc. Int. Solid Freeform Fabr. Symp.*, 2016, pp. 1145–1160.

[2] B. Yao, F. Imani, and H. Yang, "Markov decision process for image-guided additive manufacturing," *IEEE Robot. Automat. Lett.*, vol. 3, no. 4, pp. 2792–2798, Oct. 2018.

[3] B. Richter *et al.*, "High-speed X-ray investigation of melt dynamics during continuous-wave laser remelting of selective laser melted Co-Cr alloy," *CIRP Ann.*, vol. 68, no. 1, pp. 229–232, 2019.

[4] T. Furumoto, K. Egashira, K. Munekage, and S. Abe, "Experimental investigation of melt pool behaviour during selective laser melting by high speed imaging," *CIRP Ann.*, vol. 67, no. 1, pp. 253–256, 2018.

[5] H. Yang *et al.*, "Six-sigma quality management of additive manufacturing," *Proc. IEEE*, vol. 109, no. 4, pp. 347–376, Apr. 2021.

[6] C. Kan and H. Yang, "Dynamic network monitoring and control of in situ image profiles from ultraprecision machining and biomanufacturing processes," *Qual. Rel. Eng. Int.*, vol. 33, no. 8, pp. 2003–2022, 2017.

[7] L. Zhang, K. Wang, and N. Chen, "Monitoring wafers' geometric quality using an additive gaussian process model," *IIE Trans.*, vol. 48, no. 1, pp. 1–15, 2016.

[8] A. Caggiano, J. Zhang, V. Alfieri, F. Caiazzo, R. Gao, and R. Teti, "Machine learning-based image processing for on-line defect recognition in additive manufacturing," *CIRP Ann.*, vol. 68, no. 1, pp. 451–454, 2019.

[9] B. Yao, F. Imani, A. Sakpal, E. Reutzel, and H. Yang, "Multifractal analysis of image profiles for the characterization and detection of defects in additive manufacturing," *J. Manuf. Sci. Eng.*, vol. 140, no. 3, 2018, Art. no. 031014.

[10] A. Lindenmeyer, S. Webster, M. Zaeh, K. Ehmann, and J. Cao, "Template-bayesian approach for the evaluation of melt pool shape and dimension of a DED-process from in-situ X-ray images," *CIRP Ann.*, vol. 70, no. 1, pp. 183–186, 2021.

[11] L. Scime and J. Beuth, "Using machine learning to identify in-situ melt pool signatures indicative of flaw formation in a laser powder bed fusion additive manufacturing process," *Additive Manuf.*, vol. 25, pp. 151–165, 2019.

[12] Z. Yang, Y. Lu, H. Yeung, and S. Krishnamurty, "Investigation of deep learning for real-time melt pool classification in additive manufacturing," in *Proc. IEEE 15th Int. Conf. Automat. Sci. Eng.*, 2019, pp. 640–647.

[13] T. Moges, Z. Yang, K. Jones, S. Feng, P. Witherell, and Y. Lu, "Hybrid modeling approach for melt-pool prediction in laser powder bed fusion additive manufacturing," *J. Comput. Inf. Sci. Eng.*, vol. 21, no. 5, 2021, Art. no. 050902.

[14] Z. Yang, Y. Lu, H. Yeung, and S. Krishnamurty, "From scan strategy to melt pool prediction: A neighboring-effect modeling method," *J. Comput. Inf. Sci. Eng.*, vol. 20, no. 5, 2020, Art. no. 051001.

[15] Y. Chen, F. Leonelli, and H. Yang, "Heterogeneous sensing and predictive modeling of postoperative outcomes," in *Healthcare Analytics: From Data to Knowledge to Healthcare Improvement*. Hoboken, NJ, USA: Wiley, 2015, pp. 463–501.

[16] B. Lane and H. Yeung, "Process monitoring dataset from the additive manufacturing metrology testbed (AMMT): Three-dimensional scan strategies," *J. Res. Nat. Inst. Standards Technol.*, vol. 124, pp. 1–14, 2019.

[17] A. Olleak and Z. Xi, "Calibration and validation framework for selective laser melting process based on multi-fidelity models and limited experiment data," *J. Mech. Des.*, vol. 142, no. 8, 2020, Art. no. 081701.

[18] Y. Chen and H. Yang, "Sparse modeling and recursive prediction of space-time dynamics in stochastic sensor networks," *IEEE Trans. Automat. Sci. Eng.*, vol. 13, no. 1, pp. 215–226, Jan. 2016.

[19] B. Yao and H. Yang, "Physics-driven spatiotemporal regularization for high-dimensional predictive modeling: A novel approach to solve the inverse ECG problem," *Sci. Rep.*, vol. 6, 2016, Art. no. 39012.

[20] C. Kan, S. Kumara, and H. Yang, "Parallel computing and network analytics for fast internet-of-things (IoT) machine information processing and condition monitoring," *J. Manuf. Syst.*, vol. 46, no. 5, pp. 282–293, 2018.

[21] F. Imani, C. Cheng, and H. Yang, "Nested Gaussian process modeling for high-dimensional data imputation in healthcare systems," *IISE Trans. Healthcare Syst. Eng.*, vol. 9, no. 4, pp. 315–326, 2019.

[22] R. Liu, B. Vogt, and H. Yang, "Gaussian process monitoring of Layerwise-dependent imaging data," *IEEE Robot. Automat. Lett.*, vol. 6, no. 4, pp. 8029–8036, Oct. 2021.